iScience

CellPress

Article

Reversible Charge Transfer and Adjustable Potential Window in Semiconductor/Faradaic Layer/Liquid Junctions

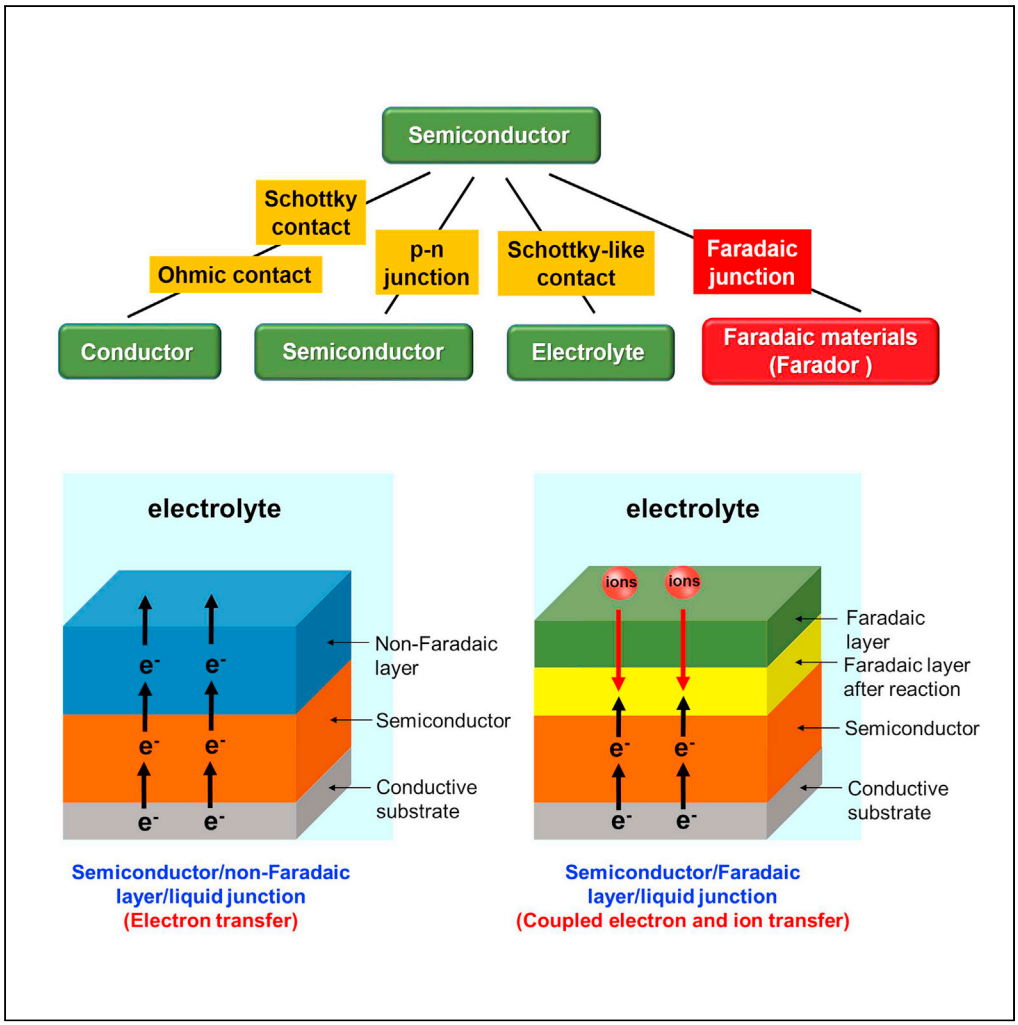

Xiangtian Chen, Kaijian Zhu, Pin Wang, Gengzhi Sun, Yingfang Yao, Wenjun Luo, Zhigang Zou

wjluo@nju.edu.cn (W.L.)
zgzou@nju.edu.cn (Z.Z.)

HIGHLIGHTS

A new concept of a Faradaic junction is proposed

The photoelectrode performance is improved by eliminating short circuit contact

A characteristic of adjustable potential window in a Faradaic junction is reported

Chen et al., iScience 23, 100949
March 27, 2020
https://doi.org/10.1016/j.isci.2020.100949

iScience

CellPress

Article

Reversible Charge Transfer and Adjustable Potential Window in Semiconductor/Faradaic Layer/Liquid Junctions

Xiangtian Chen,[1] Kaijian Zhu,[2] Pin Wang,[1] Gengzhi Sun,[3] Yingfang Yao,[2] Wenjun Luo,[2,4,*] and Zhigang Zou[1,2,*]

SUMMARY

Semiconductor/Faradaic layer/liquid junctions have been widely used in solar energy conversion and storage devices. However, the charge transfer mechanism of these junctions is still unclear, which leads to inconsistent results and low performance of these devices in previous studies. Herein, by using Fe_2O_3 and $Ni(OH)_2$ as models, we precisely control the interface structure between the semiconductor and the Faradaic layer and investigate the charge transfer mechanism in the semiconductor/Faradaic layer/liquid junction. The results suggest that the short circuit severely restricts the performance of the junction for both solar water splitting cells and solar charging supercapacitors. More importantly, we also find that the charge-discharge potential window of a Faradaic material sensitively depends on the energy band positions of a semiconductor, which provides a new way to adjust the potential window of a Faradaic material. These new insights offer guidance to design high-performance devices for solar energy conversion and storage.

INTRODUCTION

Solar energy, as a green, renewable, and widely available energy source, plays an important role in achieving a sustainable society. In the past decades, various solar energy-harvesting technologies, such as solar cells, solar water-splitting cells, and solar charging supercapacitors, have attracted intensive attention (Yao et al., 2018; Jiang et al., 2017; Shi et al., 2016; Sun and Yan, 2017; Yi et al., 2018; Sun et al., 2018; Ma et al., 2019). Among them, semiconductor/liquid junctions are core structures in these devices. Electron-hole pairs are generated in semiconductors under irradiation, which are separated and transferred across the semiconductor/liquid interface. In these processes, the efficiencies of charge separation and transfer have critical effects on the performances of these devices. In previous studies, an intermediate layer, sandwiched between semiconductor and liquid, was widely used to improve the charge separation and transfer at the semiconductor/liquid interface. Usually, there are two kinds of intermediate layers, non-Faradaic and Faradaic (see Figure 1). A non-Faradaic intermediate layer, such as TiO_2 and Al_2O_3, is inert, which is used to improve charge separation by built-in electric field (Lin et al., 2012; Boettcher et al., 2011; Luo et al., 2007) and surface passivation (Yu et al., 2017; Chen et al., 2011; Seger et al., 2013). In contrast, a Faradaic intermediate layer, such as $Ni(OH)_2$, CoPi, and $Fe_5HO_8{\cdot}3H_2O$, is electrochemically active, which captures/releases electrons from the semiconductor layer and at the same time reacts with the ions from the electrolyte to produce a new substance (Shao et al., 2018). It is worthy of note that this Faradaic reaction is fast and reversible by controlling an applied potential, which leads to the intermediate layer regenerated. In previous studies, Faradaic intermediate layers were coated on the surfaces of semiconductor photoanodes as hole collectors (Liu et al., 2014; Li et al., 2018; Laskowski et al., 2019) and oxygen evolution catalysts (Kim and Choi, 2014; Lin and Boettcher, 2014; Zhong et al., 2011; Li et al., 2013; Wang et al., 2018), which enhanced both charge separation and transfer efficiency at the semiconductor/liquid interface. Therefore, Faradaic layers are more ideal than non-Faradaic layers for high-efficiency solar water-splitting cells. However, other reports suggested that the coating of Faradaic layers on semiconductor photoanodes decreased the performance of solar water splitting (Wang et al., 2013; Lim et al., 2017; Zhu et al., 2018). Since both the semiconductors and the Faradaic layers are the same (Liu et al., 2016; Young and Hamann, 2014; Steier et al., 2015), the inconsistent results in previous studies possibly originate from uncontrollable interface structures between semiconductors and Faradaic layers.

Moreover, some Faradaic layers, including $Ni(OH)_2$ (Zhu et al., 2018; Xia et al., 2012; Wang et al., 2014) and PbO_x (Safshekan et al., 2017), have also been directly coated on the surface of semiconductors as photo charging supercapacitors for solar conversion and storage. In these devices, electron-hole pairs are

[1]Eco-materials and Renewable Energy Research Center (ERERC), Jiangsu Key Laboratory for Nano Technology, National Laboratory of Solid State Microstructures and Department of Physics, Nanjing University, Nanjing, Jiangsu 210093, China

[2]Eco-materials and Renewable Energy Research Center (ERERC), College of Engineering and Applied Sciences, Nanjing University, Nanjing, Jiangsu 210093, China

[3]Key Laboratory of Flexible Electronics (KLOFE) & Institute of Advanced Materials (IAM), Nanjing Tech University, Nanjing, Jiangsu 211816, China

[4]Lead Contact

*Correspondence: wjluo@nju.edu.cn (W.L.), zgzou@nju.edu.cn (Z.Z.)

https://doi.org/10.1016/j.isci.2020.100949

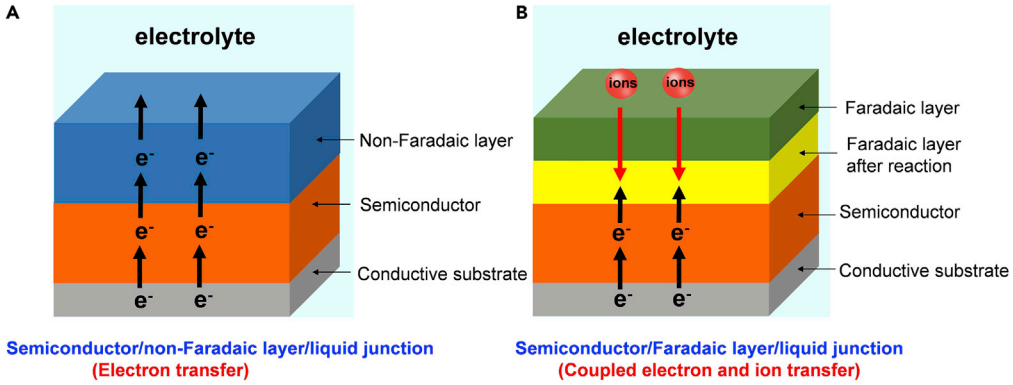

Figure 1. Schematic Diagrams of a Non-Faradaic Junction and a Faradaic Junction

Schematic diagrams of semiconductor/non-Faradaic layer/liquid junction (A) and semiconductor/Faradaic layer/liquid junction (B).

See also Figure S1.

generated in semiconductors under irradiation, which are injected into the Faradaic layers to be stored. When the light is off, the stored electrons or holes in the Faradaic layers are released as electricity. The photo charge and dark discharge are also reversible owing to the Faradaic reaction. In conventional supercapacitors, Faradaic layers on conductive substrates can be charged completely in dark. However, in solar charging supercapacitors, only a little part of Faradaic layers are photo-charged on semiconductors, which leads to much lower specific capacitances in solar charging supercapacitors than conventional supercapacitors (Zhu et al., 2018; Xia et al., 2012; Sekhar et al., 2017; Chang et al., 2014). It is not clear whether the charging processes on semiconductors are different from those on conductive substrates or not. Although semiconductor/Faradaic layer/liquid junctions (denoted as Faradaic junctions) have been used in solar water splitting cells and solar charging supercapacitors, the charge transfer mechanism is still unclear because the charge carriers in a Faradaic material are coupled electrons and ions, which are essentially different from electrons or ions in other conventional semiconductor junctions, such as p-n junctions, Schottky or Schottky-like junctions, and Ohmic contacts (see Figure S1). Therefore, it is desirable to understand the charge transfer mechanism in a Faradaic junction, not only to improve the performances of both solar water-splitting cells and solar charging supercapacitors, but also to provide possibilities to construct some new devices.

Herein, we report on a charge transfer mechanism in Faradaic junctions by controlling the Faradaic layers shorted or isolated with conductive substrates. Fe_2O_3 semiconductors and $Ni(OH)_2$ Faradaic layers were used as model materials. $Ni(OH)_2$ was selectively deposited on different positions of Fe_2O_3 nanorods by chemical bath deposition (CBD) and photoelectrodeposition (PED), and the fabricated samples are labeled as C-Fe_2O_3/$Ni(OH)_2$ and P-Fe_2O_3/$Ni(OH)_2$, respectively. We found that water oxidation reaction was completely restrained in C-Fe_2O_3/$Ni(OH)_2$ under illumination, whereas it was accelerated in P-Fe_2O_3/$Ni(OH)_2$. Moreover, only a small part of the $Ni(OH)_2$ in C-Fe_2O_3/$Ni(OH)_2$ was photoelectrochemically oxidized into NiOOH, but the $Ni(OH)_2$ in P-Fe_2O_3/$Ni(OH)_2$ was mostly oxidized into NiOOH under illumination. Further analysis suggested that the short circuit contact between the Faradaic layer and the conductive substrate was the reason for inconsistent results in solar water splitting and much lower specific capacitance in solar charging supercapacitors. By eliminating the short circuit contact, the performances of both solar water splitting cells and solar charging supercapacitors were improved remarkably. Moreover, we also found that the potential barrier heights between Faradaic materials and conductive substrates were negligible, whereas high-potential barriers formed between Faradaic materials and semiconductors, which led to the shift of a charge-discharge potential window of a Faradaic material. The potential window of a Faradaic material is a significant parameter in the construction of a supercapacitor full device (Shao et al., 2018). The barrier heights can be controlled by the band position of semiconductors, which suggests a new way to adjust the potential window of a Faradaic material by introducing a semiconductor layer.

RESULTS AND DISCUSSION

Fe_2O_3 nanorod arrays were hydrothermally grown on fluorine-doped tin oxide (FTO) substrates following previous studies (Liao et al., 2018). $Ni(OH)_2$ was coated on Fe_2O_3 nanorods by CBD and PED methods (see

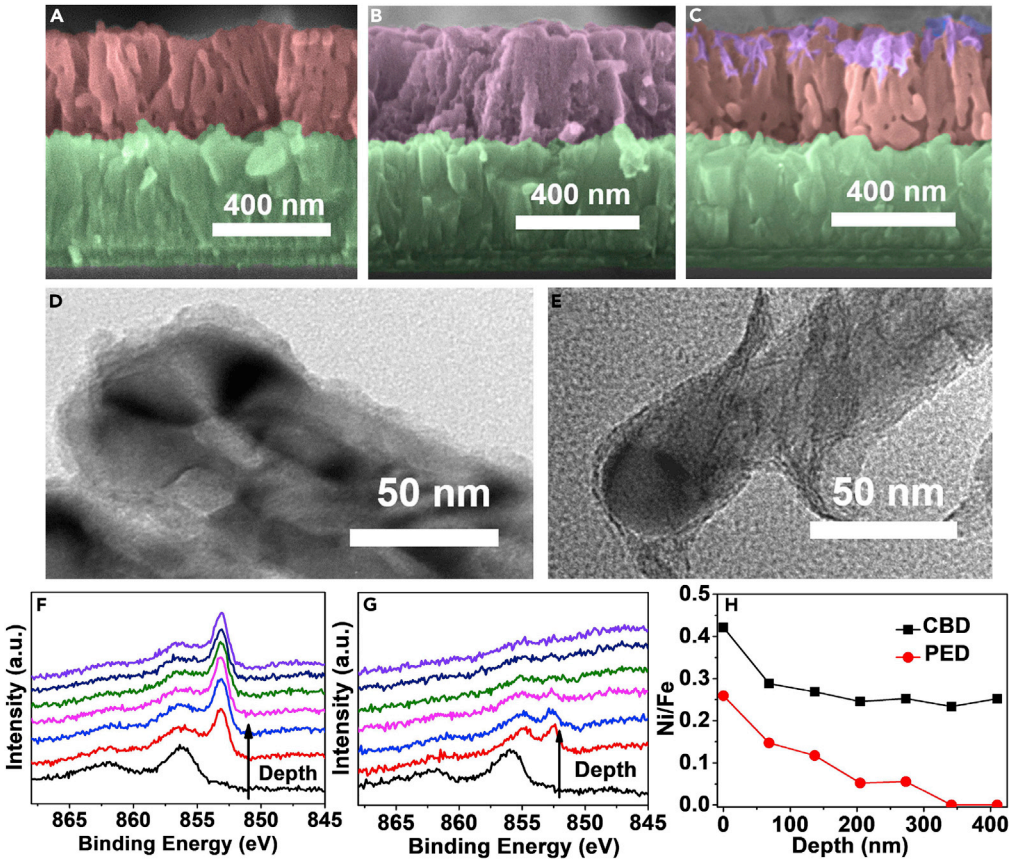

Figure 2. Characterization of Fe_2O_3 and Fe_2O_3/$Ni(OH)_2$ Electrodes

Cross-sectional SEM images for bare Fe_2O_3 (red: Fe_2O_3, green: FTO) (A), C-Fe_2O_3/$Ni(OH)_2$ (purple: $Ni(OH)_2$, green: FTO) (B), and P-Fe_2O_3/$Ni(OH)_2$ (red: Fe_2O_3, purple: $Ni(OH)_2$, green: FTO) (C); TEM images of C-Fe_2O_3/$Ni(OH)_2$ (D) and P-Fe_2O_3/$Ni(OH)_2$ (E); XPS depth profile in C-Fe_2O_3/$Ni(OH)_2$ (F) and P-Fe_2O_3/$Ni(OH)_2$ (G); the ratios of Ni/Fe at different depths of C-Fe_2O_3/$Ni(OH)_2$ and P-Fe_2O_3/$Ni(OH)_2$ (H).

See also Figures S2–S4.

Supplemental Information for details). The XRD pattern of Fe_2O_3/$Ni(OH)_2$ is shown in Figure S2. Only peaks of α-Fe_2O_3 and FTO substrates are observed. Figures 2A–2C and S3A–S3C indicate the cross-section and top-view SEM images of bare Fe_2O_3, C-Fe_2O_3/$Ni(OH)_2$, and P-Fe_2O_3/$Ni(OH)_2$, respectively. Some cavities are observed between the nanorods in bare Fe_2O_3 (see Figures 2A and S3A). After coating of $Ni(OH)_2$ on Fe_2O_3 by CBD, the whole Fe_2O_3 nanorods are covered completely by $Ni(OH)_2$, including the cavities between the nanorods, and part of the $Ni(OH)_2$ layer contacts directly with FTO substrates (see Figures 2B and S3B). In contrast, the PED process creates $Ni(OH)_2$ nanoflakes exclusively on the top of Fe_2O_3 nanorods and no $Ni(OH)_2$ contacts with FTO substrate directly (see Figures 2C and S3C). The dyeing details of the cross-section SEM image P-Fe_2O_3/$Ni(OH)_2$ are shown in Figure S4. The different deposition behaviors of $Ni(OH)_2$ in C-Fe_2O_3/$Ni(OH)_2$ and P-Fe_2O_3/$Ni(OH)_2$ samples are explained in the Supplemental Information. Moreover, TEM was also used to characterize the morphologies of these two Fe_2O_3/$Ni(OH)_2$ samples by CBD and PED, and the results are shown in Figures 2D and 2E, respectively. The C-Fe_2O_3/$Ni(OH)_2$ sample has a core-shell structure with the $Ni(OH)_2$ shell thickness of 6 nm. The surface of the P-Fe_2O_3/$Ni(OH)_2$ is covered by $Ni(OH)_2$ nanoflakes, which is in agreement with the SEM results. To further reveal the $Ni(OH)_2$ distributions, the XPS depth profile was used to analyze the samples by Ar^+ etching and the results are indicated in Figures 2F–2H. The binding energy at 856.3 eV with a satellite peak at 862.1 eV on the surfaces of the two samples by CBD and PED is assigned to Ni 2p (Ji et al., 2013; Zhu et al., 2017a, 2017b). A new peak at 853.1 eV appears at different depths of the two samples owing to the reduction of Ni^{2+} into metallic Ni by Ar^+ etching (Kim and Winograd, 1974). The intensities of XPS peaks of Ni 2p at different depths in C-Fe_2O_3/$Ni(OH)_2$ are similar, whereas the intensities in P-Fe_2O_3/$Ni(OH)_2$ become lower with the etching depths increasing until the peaks disappear. Figure 2H indicates the ratios of Ni/Fe at different

depths of C-Fe_2O_3/$Ni(OH)_2$ and P-Fe_2O_3/$Ni(OH)_2$. In C-Fe_2O_3/$Ni(OH)_2$, the ratios of Ni/Fe are almost the same at different depths except for a little higher value on the surface, which suggests that Ni^{2+} uniformly distributes in the whole Fe_2O_3 film and some $Ni(OH)_2$ contacts with FTO substrate directly. However, the ratios of Ni/Fe decrease gradually to a negligible level at the depth of 300 nm in P-Fe_2O_3/$Ni(OH)_2$, which suggests that $Ni(OH)_2$ distributes only on the top of the Fe_2O_3 film and no $Ni(OH)_2$ contacts with the FTO substrate directly.

To reveal the charge transfer mechanism in the Faradaic junction, the electrochemical and photoelectrochemical properties of C-Fe_2O_3/$Ni(OH)_2$ and P-Fe_2O_3/$Ni(OH)_2$ were measured in 1 M KOH aqueous solution. If not specifically mentioned, light is illuminated from the Fe_2O_3/$Ni(OH)_2$/electrolyte interface. As a reference sample, $Ni(OH)_2$ was first directly deposited on an FTO substrate by CBD method. In the dark, the colorless $Ni(OH)_2$ on FTO substrate becomes black after being oxidized into NiOOH at the potential of 1.46 V versus reversible hydrogen electrode (RHE) (see Figure 3A) (Zhu et al., 2017a, 2017b). The C-Fe_2O_3/$Ni(OH)_2$ becomes dark red from red at the same potential in the dark (see Figure 3B). Since the color of a bare Fe_2O_3 does not change in the dark at the same potential (see Figure S5A), the changed color comes from oxidation of $Ni(OH)_2$ in C-Fe_2O_3/$Ni(OH)_2$ by transferring electrons to FTO directly. In contrast, neither redox peak nor color change is observed on P-Fe_2O_3/$Ni(OH)_2$ at the whole potential range of 0.3 V–1.7 V versus RHE in dark (see Figure 3B), suggesting the highly chemical resistance to oxidation of $Ni(OH)_2$ in this case. Figure 3C shows the cyclic voltammetry curves of C-Fe_2O_3/$Ni(OH)_2$ with different scan rates under illumination. The C-Fe_2O_3/$Ni(OH)_2$ shows two pairs of redox peaks. When the scan rate is 10 mV/s, an oxidation peak at 0.93 V versus RHE is observed and no photocurrent is observed at the potential range of 1.1–1.3 V versus RHE. The peak intensity and width increase with increase in the scan rate, which suggests the photocurrent comes from holes-induced capacitive current (Tian et al., 2013). The color of C-Fe_2O_3/$Ni(OH)_2$ changes from red to dark red after the first oxidation peak. The color of a bare Fe_2O_3 does not change under illumination at the same potential (see Figure S5B), indicating $Ni(OH)_2$ is oxidized into NiOOH. Moreover, C-Fe_2O_3/$Ni(OH)_2$ does not change color in the dark in this range (see Figure 3B) and the photocurrent of the first peak comes from the oxidation of $Ni(OH)_2$ by photo-generated holes in Fe_2O_3. In order to further confirm that the photocurrent of the first peak does not come from water oxidation, I-t curves of C-Fe_2O_3/$Ni(OH)_2$ were also measured under illumination (see Figure 3E). The photocurrent decays quickly and negligible steady photocurrent is obtained at all selected potentials. According to previous studies (Wang et al., 2013; Zhu et al., 2018), the transient photocurrent comes from $Ni(OH)_2$ oxidation and the photocurrent will disappear once all of $Ni(OH)_2$ is oxidized into NiOOH. The steady photocurrent comes from water oxidation. When water is oxidized into O_2, some other water molecules in the electrolyte will diffuse to the electrode surface to maintain the water concentrations. Therefore, the photocurrent is stable. The present results suggest that water oxidation reaction is completely suppressed in C-Fe_2O_3/$Ni(OH)_2$. After C-Fe_2O_3/$Ni(OH)_2$ is scanned at the second peak (1.5 V versus RHE), the color of the sample becomes deeper and more $Ni(OH)_2$ is oxidized at this potential. Similar oxidation current is also observed at the same potential in FTO/$Ni(OH)_2$ in the dark (see Figure 3A). Therefore, the oxidation current of C-Fe_2O_3/$Ni(OH)_2$ at the second peak comes from electrochemical oxidation of $Ni(OH)_2$. After $Ni(OH)_2$ is mostly oxidized into NiOOH, water oxidation starts (Cibrev et al., 2013). When the light is off, two reduction peaks at 1.29 and 0.7 V versus RHE are observed in C-Fe_2O_3/$Ni(OH)_2$ (see Figure 3C). The color of C-Fe_2O_3/$Ni(OH)_2$ becomes lighter after the second reduction peak (1.29 V versus RHE). This reduction peak is very close to that of $Ni(OH)_2$ on FTO substrates (see Figure 3A), which suggests it comes from the reduction of NiOOH by electrons from the FTO substrate. However, the color of the film does not completely recover after the second reduction peak (1.29 V versus RHE), indicating some NiOOH cannot be reduced by electrons from the FTO substrate, possibly blocked by Fe_2O_3. After the first reduction peak (0.7 V versus RHE), the color of C-Fe_2O_3/$Ni(OH)_2$ completely recovers into red. The results suggest that the remaining NiOOH is reduced by electrons from Fe_2O_3.

In P-Fe_2O_3/$Ni(OH)_2$, two obvious oxidation peaks are observed when the scan rate is 10 mV/s under illumination. The first oxidation peak is at 0.8 V versus RHE. The peak intensity and width increase with increase in scan rate, which suggests that the photocurrent comes from holes-induced capacitive current (Tian et al., 2013). When the scan rates are higher (30 and 50 mV/s), the intensity of the first peak increases and the peak position shifts positively, which leads to an overlap between the first and the second peaks. The color of P-Fe_2O_3/$Ni(OH)_2$ changes from red to dark red after the first peak, indicating $Ni(OH)_2$ is oxidized into NiOOH. The second oxidation peak is very wide, and its intensity and width are independent on the scan rates. In order to further confirm the origin of the photocurrent, I-t curves of P-Fe_2O_3/$Ni(OH)_2$ were also measured at

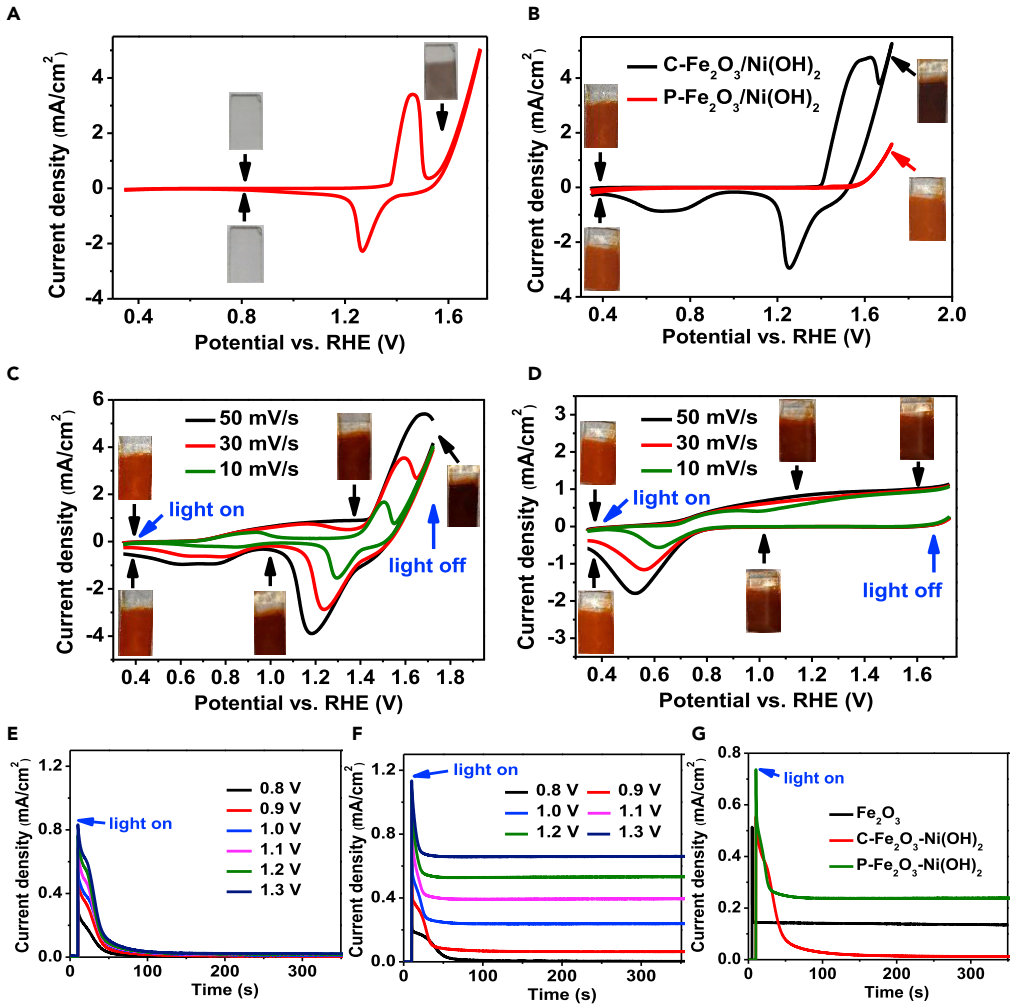

Figure 3. (Photo)electrochemical Properties of $Ni(OH)_2$, Fe_2O_3 and $Fe_2O_3/Ni(OH)_2$ Electrodes

Cyclic voltammetry (CV) curves of FTO/$Ni(OH)_2$ (A), C-Fe_2O_3/$Ni(OH)_2$, and P-Fe_2O_3/$Ni(OH)_2$ (B) in the dark; CV curves of C-Fe_2O_3/$Ni(OH)_2$ (C) and P-Fe_2O_3/$Ni(OH)_2$ (D) with different scan rates under illumination; i-t curves of C-Fe_2O_3/$Ni(OH)_2$ (E) and P-Fe_2O_3/$Ni(OH)_2$ (F) at different potentials under illumination. I-t curves of C-Fe_2O_3/$Ni(OH)_2$, P-Fe_2O_3/$Ni(OH)_2$, and bare Fe_2O_3 at 1.0 V versus RHE under illumination (G). Insets in (A–D) are the photos of FTO/$Ni(OH)_2$ or Fe_2O_3/$Ni(OH)_2$ samples at different potentials. Scan rate: 30 mV/s (if not specifically mentioned), light source: AM 1.5 G sunlight simulator, electrolyte: 1 M KOH aqueous solution.

See also Figures S5–S8 and Table S1.

different potentials under illumination (see Figure 3F). I-t curve at 0.8 V versus RHE decays to zero after about 70 s. As mentioned above, the transient photocurrent and the steady photocurrent come from $Ni(OH)_2$ oxidation and water oxidation, respectively. This result suggests that no water oxidation happens at 0.8 V versus RHE and all the photocurrent at this potential comes from Ni^{2+} oxidation. When the potential is higher than 0.9 V versus RHE, the photocurrent of P-Fe_2O_3/$Ni(OH)_2$ initially decays and then keeps constant. After $Ni(OH)_2$ is mostly oxidized into NiOOH, the photocurrent becomes stable for water oxidation. Therefore, the second peak comes from water oxidation. After the reduction peak, P-Fe_2O_3/$Ni(OH)_2$ becomes red (see Figure 3D), which suggests that NiOOH is reduced by electrons from Fe_2O_3 since no $Ni(OH)_2$ contacts with FTO directly in the sample.

Moreover, the water oxidation photocurrent of Fe_2O_3 at 1.0 V versus RHE is enhanced and its onset potential is also negatively shifted after coating $Ni(OH)_2$ (see Figures 3G and S6A). I-t curve of P-Fe_2O_3/$Ni(OH)_2$ at 1.0 V versus RHE is also measured for 3.5 h. After 0.8 h, the photocurrent gradually decays to about 80% of the initial photocurrent and then keeps stable (see Figure S6B). Cyclic voltammetry (CV) and i-t curves of

bare Fe_2O_3 and P-Fe_2O_3/$Ni(OH)_2$ were measured from front and back illumination and the results are shown in Figures S7A and S7B. Higher performance is obtained from front illumination than from back illumination, because most of $Ni(OH)_2$ distributes at the front side of Fe_2O_3 (the interface between the Fe_2O_3 and electrolyte) in P-Fe_2O_3/$Ni(OH)_2$. These results suggest that NiOOH serves as a Faradaic electrocatalyst for water oxidation, leading to a faster charge separation rate at the surface of Fe_2O_3. Water oxidation is enhanced in P-Fe_2O_3/$Ni(OH)_2$. However, it is completely suppressed in C-Fe_2O_3/$Ni(OH)_2$. In previous studies, some inconsistent results (improved or decreased water oxidation photocurrent) have been reported on $Ni(OH)_2$-coated Fe_2O_3 photoanodes (Wang et al., 2013; Lim et al., 2017; Zhu et al., 2018; Liu et al., 2016; Young and Hamann, 2014; Steier et al., 2015). According to the above analysis, it is proposed that the reasons are the different distributions of $Ni(OH)_2$ on Fe_2O_3 nanorods. If $Ni(OH)_2$ contacts with an FTO conductive substrate, the water oxidation performance of an Fe_2O_3 photoanode will be decreased. In contrast, if $Ni(OH)_2$ does not contact with an FTO conductive substrate, the water oxidation performance will be improved.

The specific capacitances of C-Fe_2O_3/$Ni(OH)_2$ and P-Fe_2O_3/$Ni(OH)_2$ as solar charging supercapacitors were measured, and the results are shown in Table S1. The experimental capacitance of $Ni(OH)_2$ in C-Fe_2O_3/$Ni(OH)_2$ is 350 C/g, only 33.7% of the theoretical value. In contrast, the experimental capacitance of $Ni(OH)_2$ in P-Fe_2O_3/$Ni(OH)_2$ is 804.6 C/g (77.4% of the theoretical value), much higher than the value in C-Fe_2O_3/$Ni(OH)_2$. The value is close to that of a conventional supercapacitor (790.3 C/g) (Shao et al., 2018). In a conventional supercapacitor, the capacitance is obtained by electrochemical charging. However, in this study, the high-capacitance supercapacitor is obtained by light charging, which can be used to store solar energy directly. Therefore, by eliminating the short circuit, the performance of a P-Fe_2O_3/$Ni(OH)_2$ electrode is significantly increased both in a solar water-splitting cell and in a solar charging supercapacitor.

An equilibrium potential is used to further understand the reversible redox process of $Ni(OH)_2$ on the two Fe_2O_3 samples by CBD and PED. At an equilibrium potential, oxidation and reduction rates of $Ni(OH)_2$ ↔ NiOOH are the same. The equilibrium potential of $Ni(OH)_2$ ↔ NiOOH is about 1.38 V versus RHE on FTO (See Figure S8A). If an applied potential is more positive than the equilibrium potential, the amount of NiOOH is higher than $Ni(OH)_2$ on the FTO substrate. In contrast, if an applied potential is more negative than the equilibrium potential, the amount of NiOOH is lower than $Ni(OH)_2$ on an FTO substrate. Notwithstanding the negative shift of $Ni(OH)_2$ ↔ NiOOH equilibrium potential from 1.38 V versus RHE to 0.74 V versus RHE on Fe_2O_3, the total equilibrium potential of $Ni(OH)_2$ ↔ NiOOH on C-Fe_2O_3/$Ni(OH)_2$ is still 1.38 V versus RHE owing to the direct contact of $Ni(OH)_2$ with an FTO substrate (see Figure 3C). However, the onset potential of dark charge is 1.37 V versus RHE (see Figure S8A), slightly lower than the total equilibrium potential of 1.38 V versus RHE. If the potential is higher than the onset potential of dark charge, the photo charge current is negligible. Therefore, only part of $Ni(OH)_2$ can be oxidized in C-Fe_2O_3/$Ni(OH)_2$ at potentials of 0.72 V–1.37 V versus RHE even under illumination. By contrast, the total equilibrium potential of $Ni(OH)_2$ ↔ NiOOH on P-Fe_2O_3/$Ni(OH)_2$ is 0.74 V versus RHE (see Figure S8B) since $Ni(OH)_2$ does not contact with an FTO conductive substrate directly. Therefore $Ni(OH)_2$ is mostly oxidized into NiOOH on P-Fe_2O_3/$Ni(OH)_2$ under illumination and then acts as Faradaic electrocatalyst for water oxidation.

Based on the above results, a general charge transfer mechanism in a Faradaic junction is proposed as follows. Figures 4A–4C show charge transfer in Fe_2O_3/$Ni(OH)_2$ Faradaic junctions during dark charge, photo charge, and dark discharge, respectively. For C-Fe_2O_3/$Ni(OH)_2$ sample during dark charge, $Ni(OH)_2$ contacts with FTO and can then be oxidized by transferring electrons to FTO (see Figure 4A). Meanwhile, $Ni(OH)_2$ releases H^+ ions into electrolyte to maintain electric neutrality. However, $Ni(OH)_2$ cannot be oxidized even at a very positive potential in P-Fe_2O_3/$Ni(OH)_2$ sample as it does not contact with FTO. There is no electron and ion transfer in P-Fe_2O_3/$Ni(OH)_2$ because there are no holes in Fe_2O_3 in the dark. When C-Fe_2O_3/$Ni(OH)_2$ is illuminated, $Ni(OH)_2$ can be photo-oxidized into NiOOH by donating electrons to Fe_2O_3, which then transfer to the FTO substrate (see Figure 4B). Noticeably, the oxidation product (NiOOH) has much lower resistance than Fe_2O_3 (see Table S2) and thereby leads to short circuit. In this condition, electrons prefer to back-transfer from FTO to NiOOH, and then reduce NiOOH to $Ni(OH)_2$, on which water oxidation reaction cannot occur, whereas for P-Fe_2O_3/$Ni(OH)_2$, in which $Ni(OH)_2$ does not contact with FTO and thus has no short circuit, electrons can only transfer from $Ni(OH)_2$ to Fe_2O_3 under illumination until $Ni(OH)_2$ is mostly photo-oxidized into NiOOH (see Figure 4B). And then NiOOH serves as Faradaic electrocatalyst for water oxidation and improves the performance of solar water splitting. The short circuit results in the poor performance in a Faradaic layer-coated photoelectrode for solar water splitting. If the short circuit exists, water oxidation reaction will be suppressed. If not, water oxidation

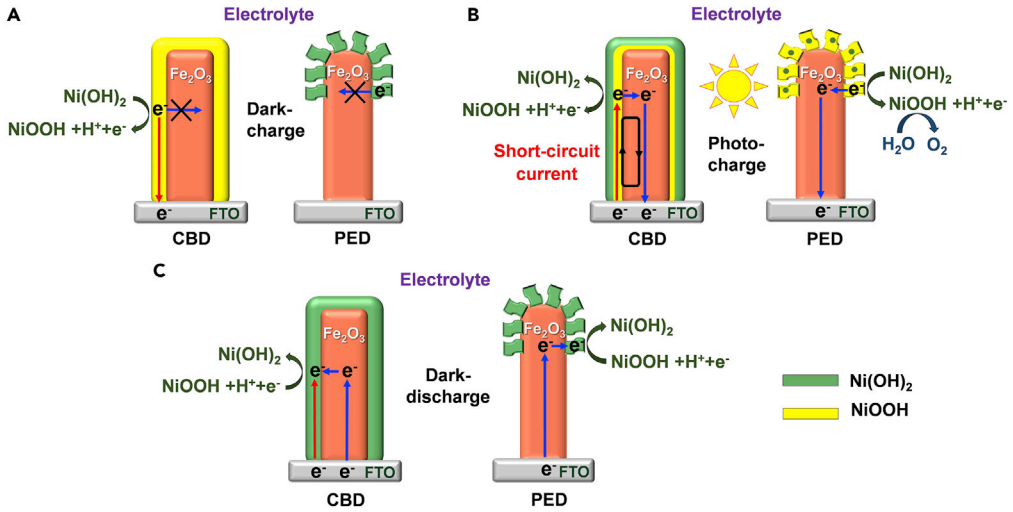

Figure 4. A Proposed Charge Transfer Mechanism in Faradaic Junctions

A proposed charge transfer mechanism in C-Fe_2O_3/$Ni(OH)_2$ and P-Fe_2O_3/$Ni(OH)_2$ during dark charge (A), photo charge (B), and dark discharge (C).

See also Table S2.

will be accelerated. This is the main reason for inconsistent results on a Faradaic layer-coated semiconductor photoelectrode for solar water splitting in previous studies (Wang et al., 2013; Lim et al., 2017; Zhu et al., 2018; Liu et al., 2016; Young and Hamann, 2014; Steier et al., 2015). Moreover, the short circuit also leads to partial oxidization of Faradaic layer in a photo-supercapacitor, which intrinsically decreases the specific capacitance. During dark discharge, there are two electron transfer paths, from Fe_2O_3 or FTO to NiOOH, in C-Fe_2O_3/$Ni(OH)_2$ (Figure 4C), which lead to two reduction peaks in CV curves (see Figure 3C), whereas in P-Fe_2O_3/$Ni(OH)_2$, electrons can only transfer from Fe_2O_3 to NiOOH and only one reduction peak is observed in CV curves (see Figure 3D).

In order to understand different charge transfer behaviors of a Faradaic layer on a conductive substrate and on a semiconductor, we also investigated the potential windows of a Faradaic layer on different conductive substrates and semiconductors. $Ni(OH)_2$ was coated on FTO, carbon paper, and Pt foil by electrodeposition (see Supplemental Information). Figure 5A shows the CV curves of FTO/$Ni(OH)_2$, C/$Ni(OH)_2$, and Pt/$Ni(OH)_2$ in the dark, respectively. Although the Fermi levels of the three conductive substrates are quite different (Andersson et al., 1998; Shin et al., 2008; Axnanda et al., 2013), the equilibrium potentials of the redox reaction ($Ni(OH)_2$ ↔ NiOOH) are still the same (1.36 V versus RHE). The galvanostatic charge-discharge (GCD) curves (see Figure 5B) also further confirm that the conductive substrates cannot change the charge-discharge potential windows of the Faradaic material by adjusting the Fermi levels of conductive substrates. Obviously different phenomena are observed on semiconductors. $Ni(OH)_2$ was coated on the top of Fe_2O_3 (P-Fe_2O_3/$Ni(OH)_2$) and TiO_2 nanorods (P-TiO_2/$Ni(OH)_2$) by the PED method, respectively. The CV curves of P-TiO_2/$Ni(OH)_2$ with sample photos at different potentials are shown in Figure S9B. Similar to P-Fe_2O_3/$Ni(OH)_2$, I-t curves of P-TiO_2/$Ni(OH)_2$ indicate transient photocurrent and steady photocurrent, which come from $Ni(OH)_2$ oxidation and water oxidation, respectively (see Figure S10). In contrast, the equilibrium potential of $Ni(OH)_2$ ↔ NiOOH (photo oxidation and dark reduction) shifts to 0.74 V versus RHE and 0.19 V versus RHE on Fe_2O_3 and TiO_2 (Figure 5C), respectively, much negative than the equilibrium potential (1.36 V versus RHE) on FTO conductive substrate. The photo oxidation peak and the dark reduction peak on P-Fe_2O_3/$Ni(OH)_2$ and P-TiO_2/$Ni(OH)_2$ are asymmetrical because part of photocurrent comes from water oxidation. Similarly, the photo charge-dark discharge potential windows of $Ni(OH)_2$ ↔ NiOOH also shift negatively on Fe_2O_3 and TiO_2 in GCD curves (Figure 5D). The potential window of a Faradaic material is the same on different conductive substrates, but it shifts remarkably on different semiconductors. This phenomenon can be explained as follows. The band positions of Fe_2O_3 and TiO_2 are obtained from the literature (Kment et al., 2017). When a Faradaic material contacts with a conductive substrate, the Fermi level of a conductive substrate is shifted to the redox potential ($Ni(OH)_2$ ↔ NiOOH) and the potential barrier height is negligible (see Figure 5E). However, on a semiconductor, a potential barrier forms and the Faradaic layer ($Ni(OH)_2$ ↔ NiOOH) is blocked from the FTO substrate by a semiconductor (Fe_2O_3 or

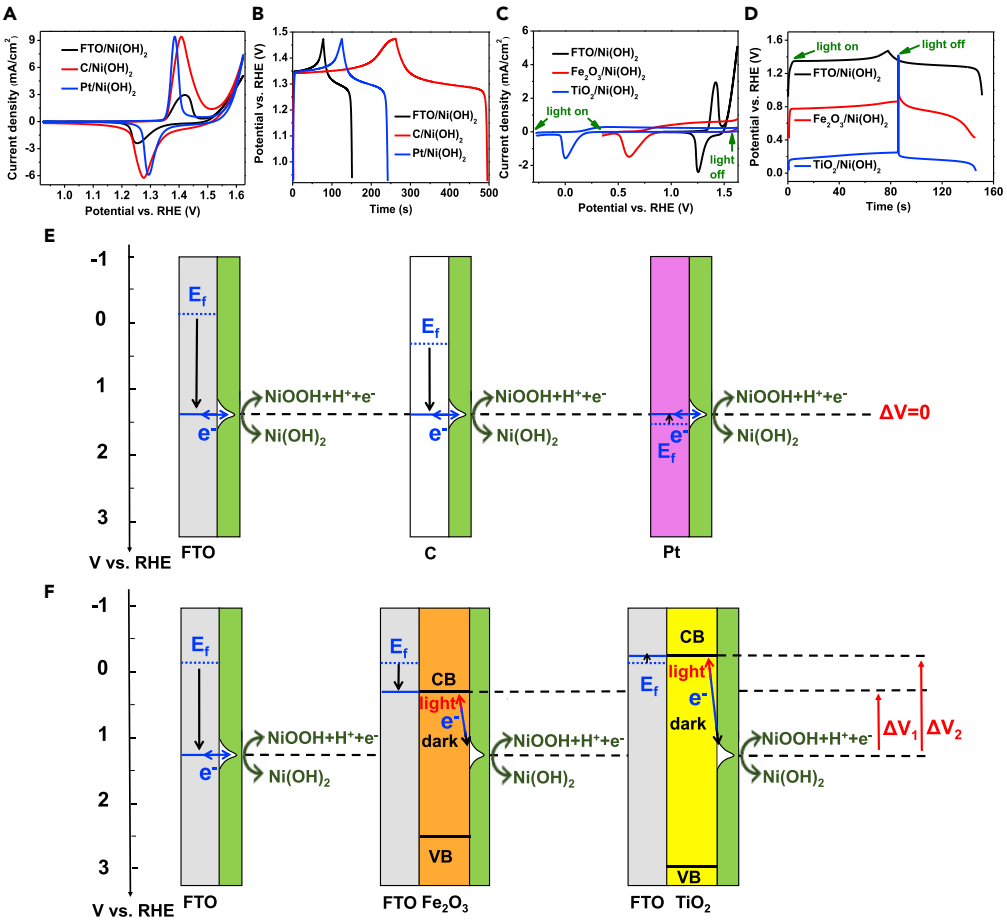

Figure 5. Different Charge Transfer Behaviors of a Faradaic Layer on a Conductive Substrate and on a Semiconductor

Cyclic voltammetry (CV) (A) and galvanostatic charge-discharge (GCD) (B) curves of $Ni(OH)_2$ on FTO, C and Pt conductive substrates with different Fermi levels in the dark; cyclic voltammetry (CV) (C) and galvanostatic charge-discharge (GCD) (D) curves of FTO/$Ni(OH)_2$, P-Fe_2O_3/$Ni(OH)_2$, and P-TiO_2/$Ni(OH)_2$ under illumination and in the dark; band diagrams of the interfaces between FTO/$Ni(OH)_2$, C/$Ni(OH)_2$, and Pt/$Ni(OH)_2$ (E) and band diagrams of the interfaces between FTO/$Ni(OH)_2$, FTO/Fe_2O_3/$Ni(OH)_2$, and FTO/TiO_2/$Ni(OH)_2$ under an applied potential (F), ΔV is the barrier height. Scan rate: 30 mV/s; light source: AM 1.5 G sunlight simulator; electrolyte: 1 M KOH aqueous solution.

See also Figures S9–S11.

TiO_2) (see Figure S11). The potential barrier height (ΔV) is the difference between the conduction band position of an n-type semiconductor and the redox potential of $Ni(OH)_2$ ↔ NiOOH. Therefore, the redox reaction of $Ni(OH)_2$ ↔ NiOOH will happen only when the conduction band position of the semiconductor shifts to the flat band position under a given negative potential (see Figure 5F). Therefore, the photo charge-dark discharge potential windows of $Ni(OH)_2$ ↔ NiOOH are adjusted by the conduction band positions of Fe_2O_3 or TiO_2. This is the first case to report on the dependence of a potential window of a Faradaic material on the energy band positions of a semiconductor, which provides guidance for designing solar charging supercapacitors. The potential windows of a positive electrode and a negative electrode are both significant for the performance of a supercapacitor full device. For a Faradaic material in a conventional supercapacitor, its electrochemical potential window is fixed. This study also suggests a new way to adjust the potential window of a Faradaic material by introducing a semiconductor layer, which provides possibilities to construct new devices.

Conclusion

A general charge transfer mechanism in a semiconductor/Faradaic layer/liquid junction was elucidated by using Fe_2O_3 and $Ni(OH)_2$ as model materials. A Faradaic layer of $Ni(OH)_2$ directly contacted with

both the semiconductor and the conductive substrate in the sample led to two kinds of electron transfer paths, one was from the semiconductor to the Faradaic layer and the other was short circuit from the conductive substrate to the Faradaic layer. The short circuit contact led to a serious decrease of the performances of both solar water-splitting cells and solar charging supercapacitors. By eliminating the short circuit contact, the performances of the devices were improved remarkably. A blocking layer can be introduced between a semiconductor and a conductive substrate to further eliminate short circuit contact and improve the performances of devices. Moreover, the potential barrier heights between Faradaic materials and conductive substrates with different Fermi levels were negligible, whereas obvious potential barrier formed between the Faradaic materials and semiconductors, which led to the shift of a potential window of a Faradaic material. The charge-discharge potential window of a Faradaic material is very important in the supercapacitor full device construction. This finding provides a new way to adjust the potential window of a Faradaic material by introducing a semiconductor layer. The Faradaic layer plays a key role in a semiconductor/Faradaic layer/liquid junction, which is a bridge between the semiconductor and the liquid to exchange charges. This work provides insight and opens up new opportunities in the rational design and development of high-performance semiconductor/Faradaic layer/liquid junctions for solar energy conversion and storage.

Limitations of the Study

In this study, by eliminating short circuit contact in a Faradaic junction photoelectrode, its performance in both solar water splitting and solar charging supercapacitors has been improved. However, the preparation method of the Faradaic layer needs to be further explored to obtain a higher mass loading. Besides, the photoelectrode as a solar charging supercapacitor was only measured in a three-electrode cell. A full device needs to be constructed in future.

METHODS

All methods can be found in the accompanying Transparent Methods supplemental file.

SUPPLEMENTAL INFORMATION

Supplemental Information can be found online at https://doi.org/10.1016/j.isci.2020.100949.

ACKNOWLEDGMENTS

The authors thank Prof. Yupeng Yuan at Anhui University and Dr. Sheng Chu at McGill University for their helpful suggestion. The authors thank Dr. Jijia Xie for conducting XPS depth characterization. This work was supported by the National Key R&D Program of China (2017YFE0120700), the National Natural Science Foundation of China (21875105), the National Scientific Instrument Development Major Project of National Natural Science Foundation of China (51627810), and the Fundamental Research Funds for the Central Universities (021314380139, 021014380115).

AUTHOR CONTRIBUTIONS

W.L. and Z.Z. proposed the project. W.L. conceived the concept and designed the experiments. X.C. prepared the samples, characterized the samples, and carried out electrochemistry measurement; W.L. and X.C. analyzed the data and wrote the paper. All authors discussed the results and gave comments on the manuscript.

DECLARATION OF INTERESTS

The authors declare no competing interests.

Received: October 30, 2019
Revised: January 11, 2020
Accepted: February 25, 2020
Published: March 27, 2020

REFERENCES

Andersson, A., Johansson, N., Broms, P., Yu, N., Lupo, D., and Salaneck, W.R. (1998). Fluorine tin oxide as an alternative to indium tin oxide in polymer LEDs. Adv. Mater. *10*, 859–863.

Axnanda, S., Scheele, M., Crumlin, E., Mao, B., Chang, R., Rani, S., Faiz, M., Wang, S., Alivisatos, A.P., and Liu, Z. (2013). Direct work function measurement by gas phase photoelectron spectroscopy and its application on PbS nanoparticles. Nano Lett. *13*, 6176–6182.

Boettcher, S.W., Warren, E.L., Putnam, M.C., Santori, E.A., Turner-Evans, D., Kelzenberg, M.D., Walter, M.G., McKone, J.R., Brunschwig, B.S., Atwater, H.A., and Lewis, N.S. (2011). Photoelectrochemical hydrogen evolution using Si microwire arrays. J. Am. Chem. Soc. *133*, 1216–1219.

Chang, I.-C., Chen, T.-T., Yang, M.-H., Chiu, H.-T., and Lee, C.-Y. (2014). Self-powered electrochemical deposition of Cu@$Ni(OH)_2$ nanobelts for high performance pseudocapacitors. J. Mater. Chem. A *2*, 10370–10374.

Chen, Y.W., Prange, J.D., Duhnen, S., Park, Y., Gunji, M., Chidsey, C.E., and McIntyre, P.C. (2011). Atomic layer-deposited tunnel oxide stabilizes silicon photoanodes for water oxidation. Nat. Mater. *10*, 539–544.

Cibrev, D., Jankulovska, M., Lana-Villarreal, T., and Gomez, R. (2013). Oxygen evolution at ultrathin nanostructured $Ni(OH)_2$ layers deposited on conducting glass. Int. J. Hydrogen Energy *38*, 2746–2753.

Ji, J., Zhang, L., Ji, H., Li, Y., Zhao, X., Bai, X., Fan, X., Zhang, F., and Ruoff, R.S. (2013). Nanoporous $Ni(OH)_2$ thin film on 3D ultrathin-graphite foam for asymmetric supercapacitor. ACS Nano *7*, 6237–6243.

Jiang, C., Moniz, S.J.A., Wang, A., Zhang, T., and Tang, J. (2017). Photoelectrochemical devices for solar water splitting-materials and challenges. Chem. Soc. Rev. *46*, 4645–4660.

Kim, K.S., and Winograd, N. (1974). X-ray photoelectron spectroscopic studies of nickel-oxygen surfaces using oxygen and argon ion-bombardment. Surf. Sci. *43*, 625–643.

Kim, T.W., and Choi, K.S. (2014). Nanoporous $BiVO_4$ photoanodes with dual-layer oxygen evolution catalysts for solar water splitting. Science *343*, 990–994.

Kment, S., Riboni, F., Pausova, S., Wang, L., Wang, L., Han, H., Hubicka, Z., Krysa, J., Schmuki, P., and Zboril, R. (2017). Photoanodes based on TiO_2 and α-Fe_2O_3 for solar water splitting–superior role of 1D nanoarchitectures and of combined heterostructures. Chem. Soc. Rev. *46*, 3716–3769.

Laskowski, F.A.L., Nellist, M.R., Qiu, J., and Boettcher, S.W. (2019). Metal oxide/(oxy) hydroxide overlayers as hole collectors and oxygen-evolution catalysts on water-splitting photoanodes. J. Am. Chem. Soc. *141*, 1394–1405.

Li, L., Yang, X., Lei, Y., Yu, H., Yang, Z., Zheng, Z., and Wang, D. (2018). Ultrathin Fe-NiO nanosheets as catalytic charge reservoirs for a planar Mo-doped $BiVO_4$ photoanode. Chem. Sci. *9*, 8860–8870.

Li, M., Luo, W., Cao, D., Zhao, X., Li, Z., Yu, T., and Zou, Z. (2013). A co-catalyst-loaded Ta_3N_5 photoanode with a high solar photocurrent for water splitting upon facile removal of the surface layer. Angew. Chem. Int. Ed. *52*, 11016–11020.

Liao, A., He, H., Tang, L., Li, Y., Zhang, J., Chen, J., Chen, L., Zhang, C., Zhou, Y., and Zou, Z. (2018). Quasi-topotactic transformation of FeOOH nanorods to robust Fe_2O_3 porous nanopillars triggered with a facile rapid dehydration strategy for efficient photoelectrochemical water splitting. ACS Appl. Mater. Interfaces *10*, 10141–10146.

Lim, H., Kim, J.Y., Evans, E.J., Rai, A., Kim, J.H., Wygant, B.R., and Mullins, C.B. (2017). Activation of a nickel-based oxygen evolution reaction catalyst on a hematite photoanode via incorporation of cerium for photoelectrochemical water oxidation. ACS Appl. Mater. Interfaces *9*, 30654–30661.

Lin, F., and Boettcher, S.W. (2014). Adaptive semiconductor/electrocatalyst junctions in water-splitting photoanodes. Nat. Mater. *13*, 81–86.

Lin, Y., Xu, Y., Mayer, M.T., Simpson, Z.I., McMahon, G., Zhou, S., and Wang, D. (2012). Growth of p-type hematite by atomic layer deposition and its utilization for improved solar water splitting. J. Am. Chem. Soc. *134*, 5508–5511.

Liu, G., Shi, J., Zhang, F., Chen, Z., Han, J., Ding, C., Chen, S., Wang, Z., Han, H., and Li, C. (2014). A tantalum nitride photoanode modified with a hole-storage layer for highly stable solar water splitting. Angew. Chem. Int. Ed. *53*, 7295–7299.

Liu, Q., Cao, F., Wu, F., Lu, H., and Li, L. (2016). Ultrathin amorphous $Ni(OH)_2$ nanosheets on ultrathin α-Fe_2O_3 films for improved photoelectrochemical water oxidation. Adv. Mater. Interfaces *3*, 1600256.

Luo, W., Yu, T., Wang, Y., Li, Z., Ye, J., and Zou, Z. (2007). Enhanced photocurrent-voltage characteristics of WO_3/Fe_2O_3 nano-electrodes. J. Phys. D Appl. Phys. *40*, 1091–1096.

Ma, P., Sun, Y., Zhang, X., Chen, J., Yang, B., Zhang, Q., Gao, X., and Yan, X. (2019). Spinel-type solar-thermal conversion coatings on supercapacitors: an effective strategy for capacitance recovery at low temperatures. Energy Storage Mater. *23*, 159–167.

Safshekan, S., Herraiz-Cardona, I., Cardenas-Morcoso, D., Ojani, R., Haro, M., and Gimenez, S. (2017). Solar energy storage by a heterostructured $BiVO_4$-PbO_x photocapacitive device. ACS Energy Lett. *2*, 469–475.

Seger, B., Pedersen, T., Laursen, A.B., Vesborg, P.C., Hansen, O., and Chorkendorff, I. (2013). Using TiO_2 as a conductive protective layer for photocathodic H_2 evolution. J. Am. Chem. Soc. *135*, 1057–1064.

Sekhar, S.C., Nagaraju, G., and Yu, J.S. (2017). Conductive silver nanowires-fenced carbon cloth fibers-supported layered double hydroxide nanosheets as a flexible and binder-free electrode for high-performance. Nano Energy *36*, 58–67.

Shao, Y., El-Kady, M.F., Sun, J., Li, Y., Zhang, Q., Zhu, M., Wang, H., Dunn, B., and Kaner, R.B. (2018). Design and mechanisms of asymmetric supercapacitors. Chem. Rev. *118*, 9233–9280.

Shi, X., Herraiz-Cardona, I., Bertoluzzi, L., Lopez-Varo, P., Bisquert, J., Park, J.H., and Gimenez, S. (2016). Understanding the synergistic effect of WO_3–$BiVO_4$ heterostructures by impedance spectroscopy. Phys. Chem. Chem. Phys. *18*, 9255–9261.

Shin, H.-J., Clair, S., Kim, Y., and Kawai, M. (2008). Electronic structure of single-walled carbon nanotubes on ultrathin insulating films. Appl. Phys. Lett. *93*, 233104.

Steier, L., Luo, J., Schreier, M., Mayer, M.T., Sajavaara, T., and Grätzel, M. (2015). Low-temperature atomic layer deposition of crystalline and photoactive ultrathin hematite films for solar water splitting. ACS Nano *9*, 11775–11783.

Sun, Y., and Yan, X. (2017). Recent advances in dual-functional devices integrating solar cells and supercapacitors. Sol. RRL *1*, 1700002.

Sun, Y., Ma, P., Liu, L., Chen, J., Zhang, X., Lang, J., and Yan, X. (2018). Solar-thermal driven self-heating of micro-supercapacitors at low temperatures. Sol. RRL *2*, 1800223.

Tian, W., Wang, X., Zhi, C., Zhai, T., Liu, D., Zhang, C., Golberg, D., and Bandoa, Y. (2013). $Ni(OH)_2$ nanosheet@Fe_2O_3 nanowire hybrid composite arrays for high-performance supercapacitor electrodes. Nano Energy *2*, 754–763.

Wang, G., Ling, Y., Lu, X., Zhai, T., Qian, F., Tong, Y., and Li, Y. (2013). A mechanistic study into the catalytic effect of $Ni(OH)_2$ on hematite for photoelectrochemical water oxidation. Nanoscale *5*, 4129–4133.

Wang, S., Chen, P., Bai, Y., Yun, J.H., Liu, G., and Wang, L. (2018). New $BiVO_4$ dual photoanodes with enriched oxygen vacancies for efficient solar-driven water splitting. Adv. Mater. *30*, 1800486.

Wang, Y., Tang, J., Peng, Z., Wang, Y., Jia, D., Kong, B., Elzatahry, A.A., Zhao, D., and Zheng, G. (2014). Fully solar-powered photoelectrochemical conversion for simultaneous energy storage and chemical sensing. Nano Lett. *14*, 3668–3673.

Xia, X., Luo, J., Zeng, Z., Guan, C., Zhang, Y., Tu, J., Zhang, H., and Fan, H.J. (2012). Integrated photoelectrochemical energy storage: solar hydrogen generation and supercapacitor. Sci. Rep. *2*, 981.

Yao, T., An, X., Han, H., Chen, J.Q., and Li, C. (2018). Photoelectrocatalytic materials for solar water splitting. Adv. Energy Mater. *8*, 1800210.

Yi, F., Ren, H., Dai, K., Wang, X., Han, Y., Wang, K., Li, K., Guan, B., Wang, J., Tang, M., et al. (2018). Solar thermal-driven capacitance enhancement of supercapacitors. Energy Environ. Sci. *11*, 2016–2024.

Young, K.M., and Hamann, T.W. (2014). Enhanced photocatalytic water oxidation efficiency with $Ni(OH)_2$ catalysts deposited on α-Fe_2O_3 via ALD. Chem. Commun. *50*, 8727–8730.

Yu, Y., Zhang, Z., Yin, X., Kvit, A., Liao, Q., Kang, Z., Yan, X., Zhang, Y., and Wang, X. (2017). Enhanced photoelectrochemical efficiency and stability using a conformal TiO_2 film on a black silicon photoanode. Nat. Energy *2*, 17045.

Zhong, D.K., Cornuz, M., Sivula, K., Grätzel, M., and Gamelin, D.R. (2011). Photo-assisted electrodeposition of cobalt–phosphate (Co–Pi) catalyst on hematite photoanodes for solar water oxidation. Energy Environ. Sci. *4*, 1759–1764.

Zhu, K., Luo, W., Zhu, G., Wang, J., Zhu, Y., Zou, Z., and Huang, W. (2017a). Interface-engineered $Ni(OH)_2$/β-like FeOOH electrocatalysts for highly efficient and stable oxygen evolution reaction. Chem. Asian J. *12*, 2720–2726.

Zhu, L., Ong, W.L., Lu, X., Zeng, K., Fan, H.J., and Ho, G.W. (2017b). Substrate-friendly growth of large-sized $Ni(OH)_2$ nanosheets for flexible electrochromic films. Small *13*, 1700084.

Zhu, K., Zhu, G., Wang, J., Zhu, J., Sun, G., Zhang, Y., Li, P., Zhu, Y., Luo, W., Zou, Z., and Huang, W. (2018). Direct storage of holes in ultrathin $Ni(OH)_2$ on Fe_2O_3 photoelectrodes for integrated solar charging battery-type supercapacitors. J. Mater. Chem. A *6*, 21360–21367.

iScience, Volume *23*

Supplemental Information

Reversible Charge Transfer and Adjustable Potential Window in Semiconductor/Faradaic Layer/Liquid Junctions

Xiangtian Chen, Kaijian Zhu, Pin Wang, Gengzhi Sun, Yingfang Yao, Wenjun Luo, and Zhigang Zou

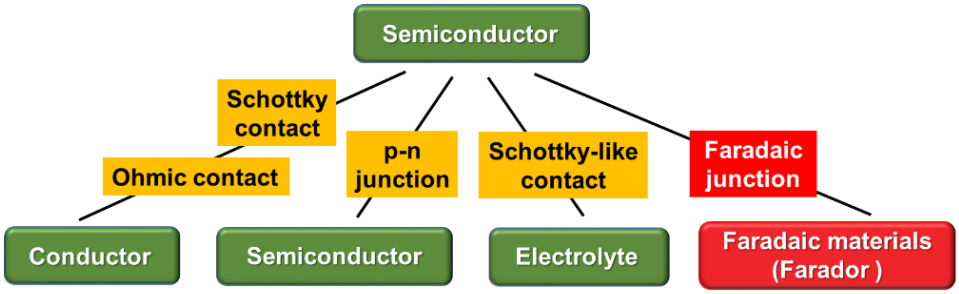

Materials	Charge carrier
Conductor	electron
Semiconductor	electron or hole
Electrolyte	ion
Farador	coupled electron and ion

Figure S1. Different kinds of semiconductor junctions. The charge carriers in different materials are also listed below. Related to Figure 1.

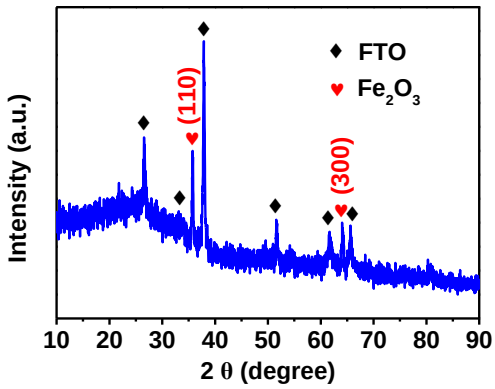

Figure S2. XRD patterns of C-Fe_2O_3/$Ni(OH)_2$. Related to Figure 2.

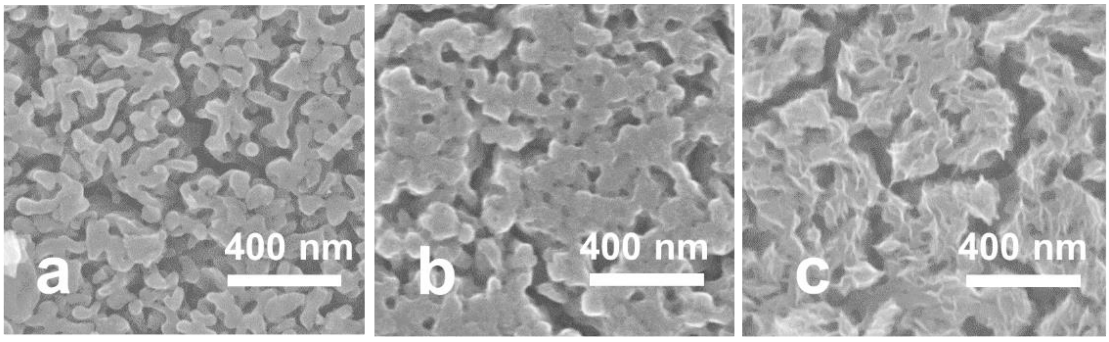

Figure S3. Top-view SEM images of bare Fe_2O_3 (a), C-Fe_2O_3/$Ni(OH)_2$ (b) and P-Fe_2O_3/$Ni(OH)_2$ (c). Related to Figure 2.

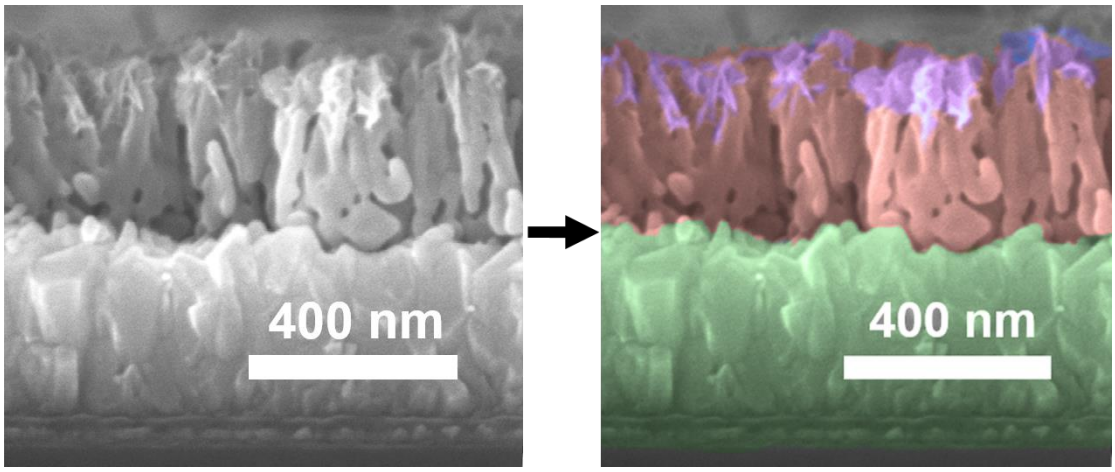

Figure S4. Dyeing details of a cross-section SEM image of P-Fe_2O_3/$Ni(OH)_2$ (red: Fe_2O_3, purple: $Ni(OH)_2$, green: FTO). Related to Figure 2.

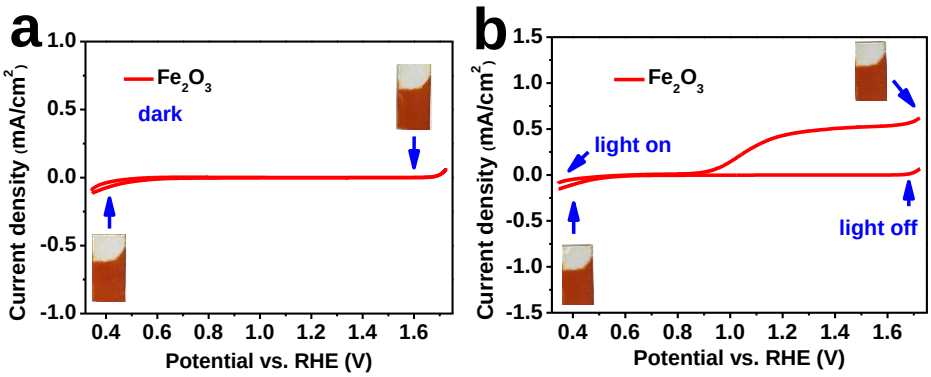

Figure S5. CV curves of bare Fe_2O_3 in dark (a) and under illumination (b). Insets are the photos of the samples at different potentials. Scan rate: 30 mV/s, Light source: AM 1.5 G sunlight simulator, electrolyte: 1 M KOH aqueous solution. Related to Figure 3.

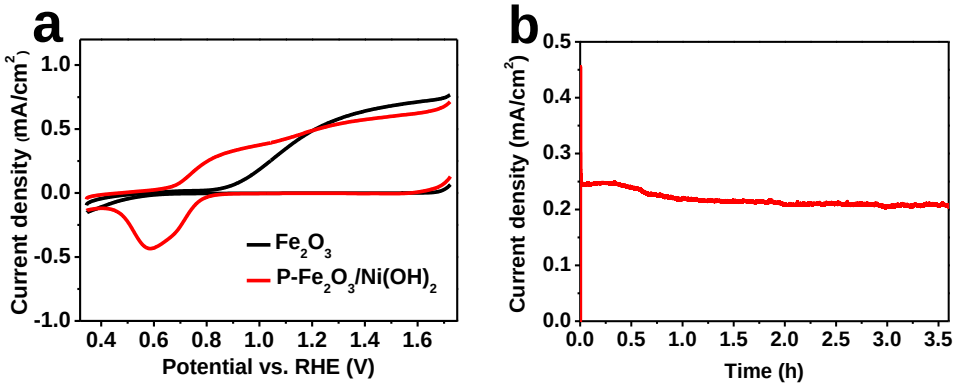

Figure S6. CV curves of P-Fe_2O_3/Ni(OH)$_2$ and bare Fe_2O_3 under illumination (a) and long-term i-t curve of P-Fe_2O_3/Ni(OH)$_2$ at 1.0 V vs. RHE (b). Scan rate: 30 mV/s, light source: AM 1.5 G sunlight simulator, electrolyte: 1 M KOH aqueous solution. Related to Figure 3.

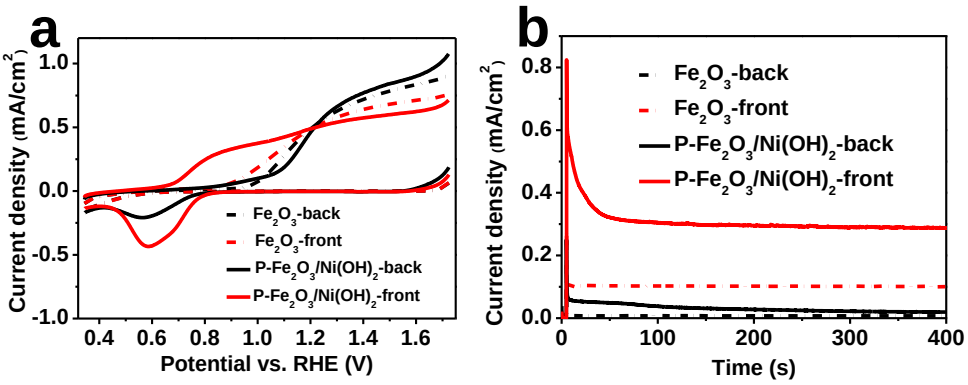

Figure S7. CV curves (a) and i-t curves at 0.9 V vs. RHE (b) of bare Fe_2O_3 and P-Fe_2O_3/Ni(OH)$_2$ under front illumination and back illumination. Light is illuminated from the Fe_2O_3/Ni(OH)$_2$/electrolyte interface under front illumination, and illuminated from the Fe_2O_3/substrate interface under back illumination.

The bare Fe_2O_3 indicates similar photocurrent-potential curves from front illumination and back illumination. However, the P-Fe_2O_3/Ni(OH)$_2$ indicates a more negative onset potential under front illumination than that under back illumination (see Figure S7a), which suggests that higher performance is obtained from front illumination than that from back illumination. The I-t curves at 0.9 V vs. RHE further confirm the sample indicates higher photocurrent from front illumination than that from back illumination (see Figure S7b). This result can be explained as follows. When illuminated from the front side, most of carriers are photo-generated at the interface between Fe_2O_3 and Ni(OH)$_2$. When illuminated from back side, most of carriers are photo-generated at the interface between Fe_2O_3 and FTO substrates, where there is less Ni(OH)$_2$. Ni(OH)$_2$ is oxidized into NiOOH and serves as electrocatalyst, which leads to higher performance. Therefore, Ni(OH)$_2$ can improve charge separation at the interface.

However, the photocurrent at high potential (1.4 V~1.6 V vs. RHE) from front illumination is lower than that of from back illumination. It is because when Ni(OH)$_2$ is mostly oxidized into NiOOH, the sample becomes black, which blocks incident light and leads to lower performance. Thererfore, the Ni(OH)$_2$ layer decreases charge generation in a photoelectrode. Related to Figure 3.

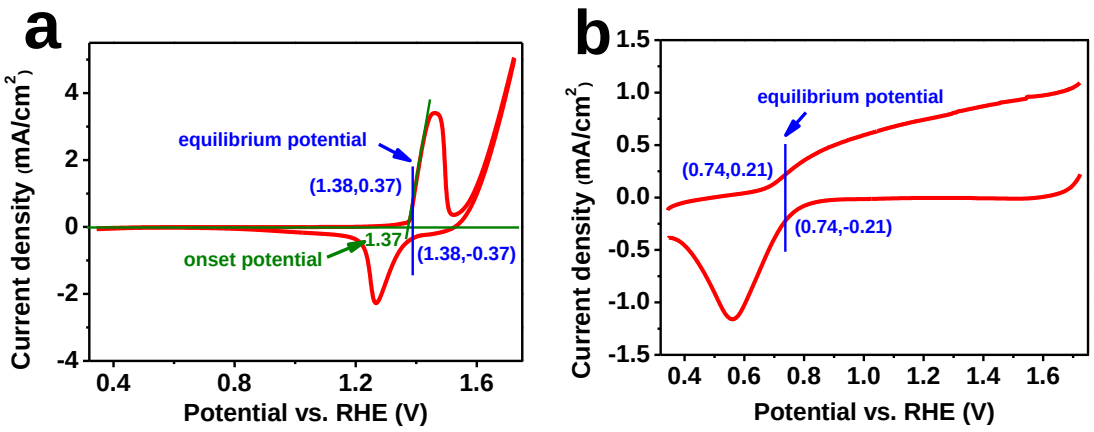

Figure S8. Schematic diagrams to estimate an equilibrium potential and an onset potential from CV curves of FTO/$Ni(OH)_2$ (a) and P-Fe_2O_3/$Ni(OH)_2$ (b). Equilibrium potentials in this article are all obtained by selecting a potential at which the oxidation current equals to the reduction current of $Ni(OH)_2 \leftrightarrow$ NiOOH. An onset oxidation potential is estimated from the intercept by extrapolating the linear region of the oxidation peak to zero current density. Related to Figure 3.

Table S1. The loading masses of $Ni(OH)_2$, experimental and theoretical specific capacitance of $Ni(OH)_2$ in C-Fe_2O_3/$Ni(OH)_2$ and P-Fe_2O_3/$Ni(OH)_2$. Related to Figure 3.

Samples	The loading mass of $Ni(OH)_2$	Experimental specific capacitance (C_E)	Theoretical specific capacitance (C_T)	C_E/C_T
CBD	30 μg/cm^2	350 C/g	1039.2 C/g	33.7%
PED	8.7 μg/cm^2	804.6 C/g	1039.2 C/g	77.4%

Table S2. The electronic conductivities of FTO, α-Fe_2O_3, TiO_2, $Ni(OH)_2$ and NiOOH from literatures. Related to Figure 4.

Materials	Electronic conductivity	References
FTO	1×10^{3} $\Omega^{-1}\cdot cm^{-1}$	Benhaoua et al., 2014
α-Fe_2O_3	10^{-14} $\Omega^{-1}\cdot cm^{-1}$	Lee et al., 2012
TiO_2	10^{-6} $\Omega^{-1}\cdot cm^{-1}$	Dy et al., 2010
$Ni(OH)_2$	10^{-13} $\Omega^{-1}\cdot cm^{-1}$	Deabate et al., 2003
NiOOH	1 $\Omega^{-1}\cdot cm^{-1}$	Tuomi et al., 1965

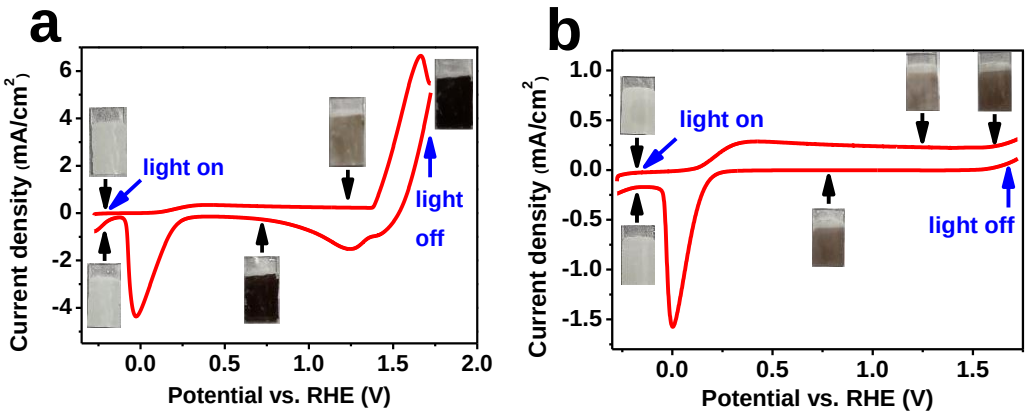

Figure S9. CV curves of C-TiO_2/$Ni(OH)_2$ (a) and P-TiO_2/$Ni(OH)_2$ (b) under illumination. Insets are the photos of the samples at different potentials. Scan rate: 30 mV/s, light source: AM 1.5 G sunlight simulator, electrolyte: 1 M KOH aqueous solution. Related to Figure 5.

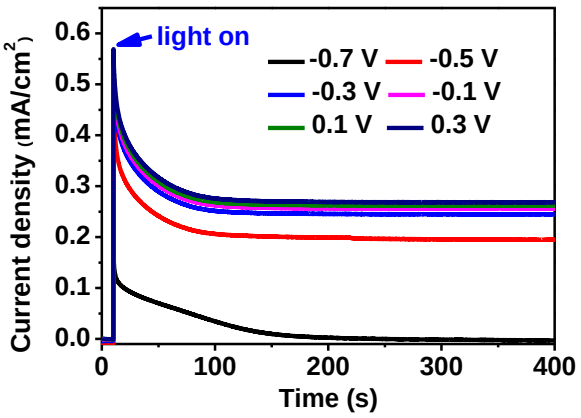

Figure S10. I-t curves of P-TiO_2/$Ni(OH)_2$ under illumination at different potentials under illumination. Light source: AM 1.5 G sunlight simulator, Electrolyte: 1 M KOH aqueous solution. Related to Figure 5.

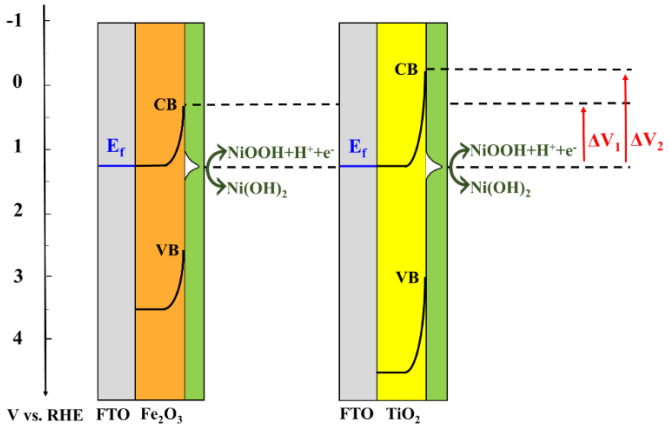

Figure S11. The band diagrams of the interfaces between FTO/Fe_2O_3/$Ni(OH)_2$ and FTO/TiO_2/$Ni(OH)_2$ without applied potential. Related to Figure 5.

Transparent Methods

Preparation of Ti-doped Fe_2O_3 nanorod films

Ti-doped Fe_2O_3 nanorod films were prepared by a hydrothermal method. Typically, the precursor solution was prepared by dissolving 0.012 mol $FeCl_3$•$6H_2O$, 0.024 mol urea and 80 μL $TiCl_3$ (15.0~20.0% $TiCl_3$ in 30% HCl) into 80 mL ultrapure water by magnetic stirring. Afterwards, the precursor solution was transferd into a 100 mL Teflon-lined stainless steel autoclave with FTO substrates in it. FeOOH films were deposited on the FTO substrates after hydrothermal reaction at 100 ^oC for 6 h in an electric oven, and washed with deionized water. The Ti-doped Fe_2O_3 nanorod films were obtained after the FeOOH films were calcined at 250 ^oC for 10 min, subsequent 550 ^oC for 120 min and then 650 ^oC for 30 min in air.

Preparation of TiO_2 nanorod films

TiO_2 nanorod films were also prepared on FTO substrates by a hydrothermal method. The precursor solution was obtained by mixing 0.45 mL titanium butoxide, 15 mL HCl and 15 mL H_2O. The solution was transferred to a Teflon-lined stainless steel autoclave with FTO substrates in it. After hydrothermal reaction at 150 ^oC for 9 h, the deposited films were rinsed by deionized water and calcined at 450 ^oC for 1 h in air to obtain TiO_2 nanorod films.

Deposition of $Ni(OH)_2$

$Ni(OH)_2$ was grown on Fe_2O_3 and TiO_2 nanorod films by chemical bath deposition method (CBD) and photoelectrodeposition (PED) method, respectively. For a CBD method, $Ni(OH)_2$ was grown on FTO, Fe_2O_3 and TiO_2 nanorod films in phosphate buffer solution containing 0.03M $Na_2S_2O_8$ and 0.02 M $Ni(NO3)_2•6H_2O$ at 70 ^oC for 10 min. For a PED method, $Ni(OH)_2$ was photoelectron-deposited at 0.35 V vs. Hg/HgO for Fe_2O_3 and -0.15 V vs. Hg/HgO for TiO_2 in 0.1 M $Ni(SO_4)_2•6H_2O$ aqueous solution with pH=7.0 (adjusted by 0.1 M KOH) under front illumination, respectively. The deposition charges on Fe_2O_3 and TiO_2 nanorod films were both 9 mC/cm^2. $Ni(OH)_2$ was also grown on FTO, carbon paper substrates and Pt in 0.1 M $Ni(SO_4)_2•6H_2O$ aqueous solution with pH=7.0 (adjusted by 0.1 M KOH) by electrodeposition. The deposition potential was -0.7 V vs. Hg/HgO and the deposition charge was 70 mC/cm^2.
The different deposition behaviors of $Ni(OH)_2$ in C-Fe_2O_3/$Ni(OH)_2$ and P-Fe_2O_3/$Ni(OH)_2$ samples are explained as follows. A CBD method is a solution reaction process, in which Ni^{2+} ions can spontaneously siege Fe_2O_3 nanorods and generate the full coverage of $Ni(OH)_2$ layer. Comparably, for a PED method, NiOOH is firstly deposited on the surface of Fe_2O_3 nanorods by photo-oxidation of Ni^{2+} under front illumination, and then electrochemically reduced to $Ni(OH)_2$ in the dark. Therefore, $Ni(OH)_2$ was deposited only on the top of Fe_2O_3 nanorods as most of holes were excited there.

Characterization of samples

SEM (Nano Nova S230) and TEM (Tecnai G2 F20) were employed to investigate the morphologies of the samples. The depth profiles of different ions in the samples were characterized by X-ray photoelectron spectroscopy (XPS) (Thermo Scientific XPS K-alpha) using Ar ion sputter gun. The binding energies were calibrated by C 1s (284.8 eV). The loading masses of $Ni(OH)_2$ were measured by inductively coupled plasma-optical emission spectroscopy (ICP-OES).

Electrochemical measurements

The electrochemical and photoelectrochemical properties of the samples were investigated in a three-electrode cell. A Pt mesh and a Hg/HgO electrode were used as a counter electrode and a reference electrode, respectively. The electrochemical measurements including cyclic voltammetry (CV) curves and Galvanostatic charge-discharge (GCD) curves were both carried out on an electrochemical workstation (Chenhua, Shanghai, CHI 760E). The electrolyte was 1 M KOH aqueous solution with pH=14. A reversible hydrogen electrode (RHE) potential was obtained by the formula: E(V vs. RHE)=E(V vs. Hg/HgO) + 0.098V + 0.059×pH. The experimental and theoretical specific capacitances are calculated using Equation (1) and (2), respectively, where Q_E and Q_T are the experimental and theoretical specific capacitances respectively, i is the discharging current density, Δt is the discharging time, $m_{Ni(OH)_2}$ is the

loading mass of $Ni(OH)_2$, $M_{Ni(OH)_2}$ is the relative molecular mass of $Ni(OH)_2$, and N_A is the Avogadro constant.

$$Q_E = \frac{i \times \Delta t}{m_{Ni(OH)_2}} \quad (1)$$

$$Q_T = \frac{m_{Ni(OH)_2} \times N_A}{M_{Ni(OH)_2} \times 6.25 \times 10^{18}} \quad (2)$$

Supplemental References

Benhaoua, A., Rahal, A., Benhaoua, B., and Jlassi, M. (2014). Effect of fluorine doping on the structural, optical and electrical properties of SnO_2 thin films prepared by spray ultrasonic. Superlattices Microstruct. *70*, 61-69.

Deabate, S., Henn, F., Devautour, S., and Giuntini, J. C. (2003). Conductivity and dielectric relaxation in various $Ni(OH)_2$ samples. J. Electrochem. Soc. *150*, 23-31.

Dy, E., Hui, R., Zhang, J., Liu, Z.-S., and Shi, Z. (2010). Electronic conductivity and stability of doped Titania ($Ti_{1-x}M_xO_2$, M=Nb, Ru, and Ta)—a density functional theory-based comparison. J. Phys. Chem. C *114,* 13162-13167.

Lee, K. K., Deng, S., Fan, H. M., Mhaisalkar, S., Tan, H. R., Tok, E. S., Loh, K. P., Chin, W. S., and Sow, C. H. (2012). α-Fe_2O_3 nanotubes-reduced graphene oxide composites as synergistic electrochemical capacitor materials. Nanoscale *4*, 2958-2961.

Tuomi D., The forming process in nickel positive electrodes. (1965). J. Electrochem. Soc. *112*, 1-12.